


Singularities in Hessian element distributions of amorphous media

Vishnu V. Krishnan^{✉,*}, Smarajit Karmakar^{✉,†} and Kabir Ramola^{✉,‡}

Centre for Interdisciplinary Sciences, Tata Institute of Fundamental Research, Hyderabad 500046, India

 (Received 4 May 2020; revised 11 September 2020; accepted 15 October 2020; published 4 November 2020)

We show that the distribution of elements H in the Hessian matrices associated with amorphous materials exhibit singularities $P(H) \sim |H|^\gamma$ with an exponent $\gamma < 0$, as $|H| \rightarrow 0$. We exploit the rotational invariance of the underlying disorder in amorphous structures to derive these exponents exactly for systems interacting via radially symmetric potentials. We show that γ depends only on the degree of smoothness n of the potential of interaction between the constituent particles at the cut-off distance, independent of the details of interaction in both two and three dimensions. We verify our predictions with numerical simulations of models of structural glass formers. Finally, we show that such singularities affect the stability of amorphous solids, through the distributions of the minimum eigenvalue of the Hessian matrix.

DOI: [10.1103/PhysRevResearch.2.042025](https://doi.org/10.1103/PhysRevResearch.2.042025)

Introduction. Understanding and modeling the properties of amorphous solids such as glasses has remained a challenge due to their extreme nonequilibrium nature as well as the underlying disorder in the arrangement of particles [1–10]. An important aspect in the study of such systems is their vibrational properties, typically probed through the eigenvalues of the Hessian matrix [11–13], with low-frequency modes being particularly relevant at the low temperatures where glass physics dominates [13–28]. Since glass-forming systems settle into disordered configurations, random matrix treatments provide a natural framework with which to model amorphous systems [29–39]. The Hessian is thus naturally characterized by the distribution of its elements [40,41]. Although the Hessian matrix is relatively simple to compute in simulations [42,43], an experimental determination remains difficult, accessible for example, only through displacement correlations in colloidal glasses [44]. In this context, it is important to study the vibrational properties of model systems via simulations. Simulation models vary in strength and range of interaction [45], and exhibit a wide range of physical properties [46]. Even though there are indications of an underlying “amorphous order” in such systems [9,10], their behavior differs fundamentally from that of crystals, with the low-lying eigenvalues of their Hessian matrices displaying marked non-Debye behavior [21–27], related to the growth of a structural length scale [47] as well as static correlations [48]. The distribution of elements affects the eigenvalues of the

Hessian which is directly related to the mechanical properties of amorphous solids [49–51].

In this Rapid Communication, we analyze the distributions of Hessian elements in structural glass formers analytically, as well as through numerical simulations. In simulations, interaction potentials are typically cut off at a finite distance for computational expediency, and in order to avoid unphysical changes, they are smoothed to relevant degrees at this cut-off [52]. However, the effect of this smoothness on vibrational properties of such amorphous systems has never been investigated. In crystals, the ordered interparticle distances imply delta distributed Hessian elements. For example, in a triangular lattice of particles with nearest-neighbor interactions as shown in Fig. 1(a), the diagonal Hessian elements take on one of two nonzero values. However, in the case of a disordered arrangement derived from simulations of glass formers as shown in Fig. 1(b), this distribution is continuous, peaking at zero with a marked singularity. We exploit the rotational invariance of the underlying amorphous disorder to derive analytic expressions for these distributions, for systems with radially symmetric interactions, which we then verify using direct numerical simulations. We show that these distributions indeed exhibit smoothness-dependent singularities

$$P(H) \sim |H|^\gamma, \quad \text{for } |H| \rightarrow 0 \quad (1)$$

with a power $\gamma < 0$. We derive exact results for γ , for any degree of smoothness, in both two dimensions (2D) as well as three dimensions (3D). Our results are summarized in Table I, highlighting the nontrivial dependence of these distributions on the nature of the interaction at the cutoff. Finally, we show that these singularities have crucial implications for the low-energy vibrational modes of amorphous systems, through a numerical sampling of the minimum eigenvalue of systems with varying smoothness in their interactions.

Distribution of Hessian elements. We begin with a disordered arrangement of particles at positions $\{\mathbf{r}^i\}$, where the particle index $i \in \{1, \dots, N\}$. The Hessian is then a $dN \times dN$ matrix where d represents the dimension of the system, with

*vishnuvk@tifrh.res.in

†smarajit@tifrh.res.in

‡kramola@tifrh.res.in

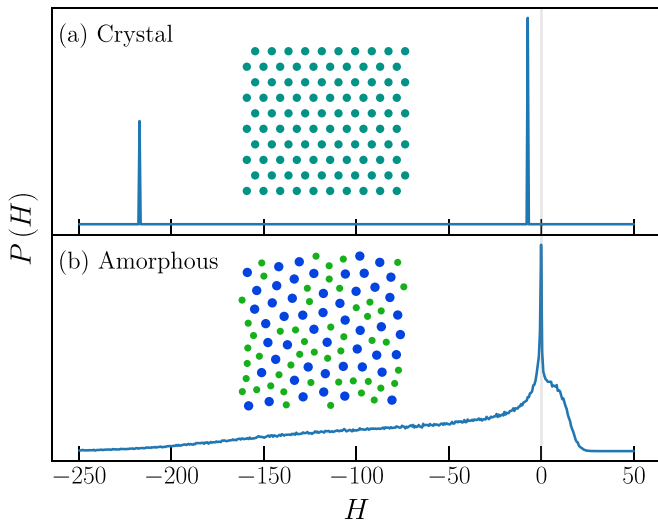


FIG. 1. Comparison of energy minimized configurations in (a) a monodisperse crystal and (b) an amorphous glass consisting of two types of particles: A (small, green) and B (large, blue). Also plotted are the corresponding distributions $P(H)$ of the diagonal elements of their Hessians. In (b), the distribution is shown only for A-B interactions.

elements $\mathcal{H}_{\alpha\beta}^{ij}$ that describe the stiffness between particles i and j , along the coordinates $\alpha, \beta \in \{x, y, z\}$. In terms of the interparticle distance vector $\mathbf{r}^{ij} = \mathbf{r}^i - \mathbf{r}^j$, the Hessian elements may be expressed as

$$\mathcal{H}_{\alpha\beta}^{ij}(\mathbf{r}^{ij}) = \frac{\partial^2 U[\{\mathbf{r}^i\}]}{\partial r_{\alpha}^{ij} \partial r_{\beta}^{ij}}. \quad (2)$$

Here, $U[\{\mathbf{r}^i\}]$ is the total potential energy of the system, which is a function of the positions of all particles. For pairwise additive interactions, $U[\{\mathbf{r}^i\}] = \sum_{ij} \psi^{ij}$, where ψ^{ij} is the interaction potential between particles i and j . We consider central potentials $\psi(r)$, where $r \equiv r^{ij} = |\mathbf{r}^{ij}|$ is the distance between particles i and j . In addition, these potentials are smoothed to n derivatives at a cut-off distance r_c , i.e., $\frac{d^m \psi}{dr^m}|_{r_c} = 0$ for all $0 \leq m \leq n$. Figure 2 shows a typical interaction potential in 2D used in our numerical simulations, and its

TABLE I. Asymptotic behavior of Hessian element distributions in the limit $H \rightarrow 0$. The diagonal element distribution depends on the relative signs of H and the interaction potential near the cutoff $\psi_{\delta} \equiv \psi(r_c - \delta)$. The results are identical for both two and three dimensions.

Element (H)	Smoothness (n)	$\lim_{H \rightarrow 0} P(H)$
Diagonal ($\alpha = \beta$)	$[2, \infty)^a$	$ H ^{-1+(3/2n)}$
	$\{2\}^b$	$ H ^{-1+(3/2n)}$
	$\{3\}^b$	$ H ^{-1/2} \log(H ^{-1})$
	$(3, \infty)^b$	$ H ^{-1+(1/(n-1))}$
Off-diagonal ($\alpha \neq \beta$)	$\{2\}$	$\log(H ^{-1})$
	$(2, \infty)$	$ H ^{-1+(1/(n-1))}$

^aCorresponds to $H \times \psi_{\delta} > 0$.

^bCorresponds to $H \times \psi_{\delta} < 0$.

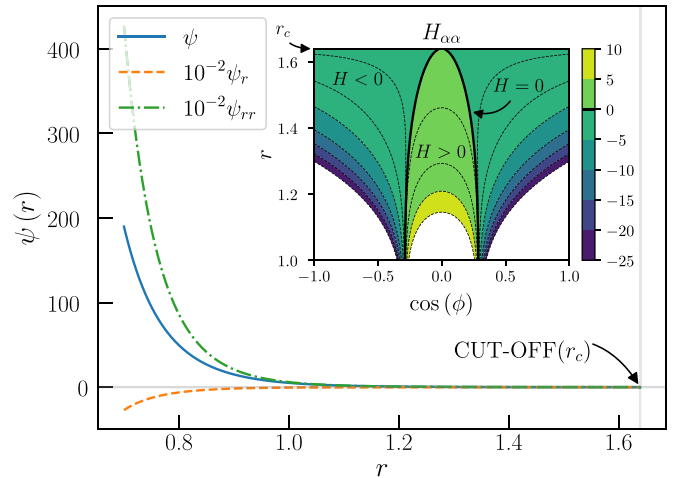


FIG. 2. The R10 potential $\psi(r) \sim r^{-10} + c + br^2 + ar^4$ for A-B interactions, smoothed to two derivatives ($n = 2$) at the cutoff [$\psi(r_c) = \psi'(r_c) = \psi''(r_c) = 0$]. The derivatives have been scaled down by a factor of 100 for clarity. The inset shows a plot in the interparticle coordinates $(r, \cos \phi)$, displaying contours which contribute to the distribution of diagonal Hessian elements ($\alpha = \beta$) at a fixed H .

derivatives, all of which tend to zero at cutoff ($n = 2$ in this case). The Hessian elements for central potentials are given by [53]

$$\mathcal{H}_{\alpha\beta}^{ij}(\mathbf{r}^{ij}) = -\left(\frac{\psi_{rr}^{ij}}{(r^{ij})^2} - \frac{\psi_r^{ij}}{(r^{ij})^3}\right)r_{\alpha}^{ij}r_{\beta}^{ij} - \delta_{\alpha\beta}\frac{\psi_r^{ij}}{r^{ij}}, \quad (3)$$

where the subscripts of r indicate partial derivatives with respect to the interparticle distances: $\psi_r \equiv \psi_r^{ij} = \partial_{r^{ij}} \psi^{ij}$, $\psi_{rr} \equiv \psi_{rr}^{ij} = \partial_{r^{ij}} \partial_{r^{ij}} \psi^{ij}$. Since the potential and its derivatives vanish at the cut-off distance, the small Hessian elements arise primarily due to pair distances near this cutoff. The values of Hessian elements in Eq. (3) depend on the length and angle of the interparticle distances in an arbitrarily chosen (fixed) Cartesian coordinate system. We therefore define a generalized angular coordinate Ω with respect to these fixed axes, which is a function of the angle ϕ in 2D, and both the polar and azimuthal angles θ, ϕ in 3D. The distribution of Hessian elements $P(H)$ is then given by

$$P(H) = \int dr d\Omega P(r, \Omega) \delta[H - \mathcal{H}_{\alpha\beta}^{ij}(\mathbf{r}^{ij})], \quad (4)$$

where $P(r, \Omega)$ represents the joint probability distributions of interparticle distances and orientations, as shown in the inset of Fig. 3. For a given H , the delta function constraint in Eq. (4) selects the corresponding contour in (r, Ω) through Eq. (3), as shown in the inset of Fig. 2.

We next exploit the rotational invariance of the underlying amorphous disorder to relate $P(H)$ to the distribution of interparticle distances. This microscopic rotational symmetry leads to isotropic angular distributions at all distances. Hence, we may assume the distributions of interparticle distances and angles to be uncorrelated $P(r, \Omega) = P(r)P(\Omega)$. Numerical sampling of this joint distribution $P(r, \Omega)$ in structural glass formers (inset of Fig. 3), demonstrates that all orientations are sampled uniformly, independent of the radial distance.

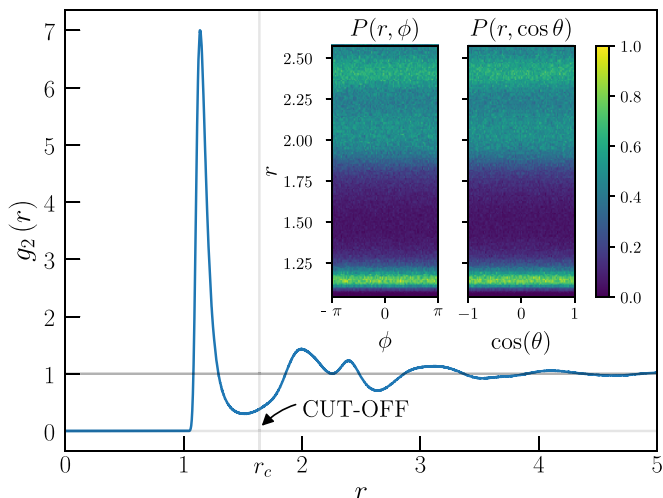


FIG. 3. Numerically sampled radial distribution function of A-B particle pairs in the R10 system in three dimensions. The vertical line indicates the cut-off distance of the interaction. Inset: Numerically sampled joint distributions of the distances (r) and angles (ϕ and $\cos \theta$), indicating isotropic angular distributions.

We therefore assume uniform distributions in the angular variables $P_{2D}(\phi) = P_{3D}(\phi) = \frac{1}{2\pi}$, and $P_{3D}(\cos \theta) = \frac{1}{2}$. The distribution of r is the radial distribution function $g_2(r)$, normalized over the range of interaction $r \in [0, r_c]$, i.e., $P(r) = g_2(r)\Theta(r_c - r)\mathcal{N}$, where Θ is the Heaviside function, and $\mathcal{N}^{-1} = \int_0^{r_c} g_2(r) dr$ is a constant of normalization. For a given H , the integration over the angular variables in Eq. (4) yields a Jacobian factor, leading to the Hessian element distribution

$$P(H) = \int_0^{r_c} dr P(r) \frac{P(\Omega)}{\left| \frac{\partial H}{\partial \Omega} \right|} = \int_0^{r_c} dr P(r) \mathcal{P}(H, r). \quad (5)$$

Above, the angular variable Ω in the final expression has been expressed in terms of H and r using Eq. (3). Therefore, given an empirical $g_2(r)$, $P(H)$ can be determined exactly. The partial integrand $\mathcal{P}(H, r) = \left[\left| \frac{\partial H}{\partial \Omega} \right| \right]^{-1} P(\Omega)$ depends on the dimension, as well as the spatial indices α and β . However, rotational symmetry dictates that there are only two classes of Hessian element distributions: the diagonal ($H_{\alpha\alpha} : H_{xx} \equiv H_{yy} \equiv H_{zz}$) and off-diagonal ($H_{\alpha\beta} : H_{xy} \equiv H_{yz} \equiv H_{zx}$).

Exact partial integrands. We first consider the distribution of Hessian elements in 2D systems, choosing the diagonal element H_{xx} and the off-diagonal element H_{xy} . From Eq. (3), $H_{xx}^{2D} = -(\psi_{rr} - \frac{\psi_r}{r}) \cos^2 \phi - \frac{\psi_r}{r}$, and $H_{xy}^{2D} = -(\psi_{rr} - \frac{\psi_r}{r}) \cos \phi \sin \phi$. It is convenient to use the angular variable $\Omega \equiv \cos \phi$ with the distribution $P_{2D}(\Omega) = 1/(\pi\sqrt{1-\Omega^2})$. Substitution of these into the expression in Eq. (5) yields the same partial integrand for both cases $\mathcal{P}_{\alpha\beta}^{2D} = [\pi \left| \frac{\partial H}{\partial \cos \phi} \right| \sqrt{1 - \cos^2 \phi}]^{-1}$. Finally, inverting the above expressions for H_{xx}^{2D} and H_{xy}^{2D} to express $\cos \phi$ in terms of H and r , we arrive at

$$\mathcal{P}_{\alpha\beta}^{2D}(H, r) = \begin{cases} |4\pi^2(H + \frac{\psi_r}{r})(H + \psi_{rr})|^{-1/2} & \alpha = \beta, \\ |\pi^2\{(\psi_{rr} - \frac{\psi_r}{r})^2 - 4H^2\}|^{-1/2} & \alpha \neq \beta. \end{cases} \quad (6)$$

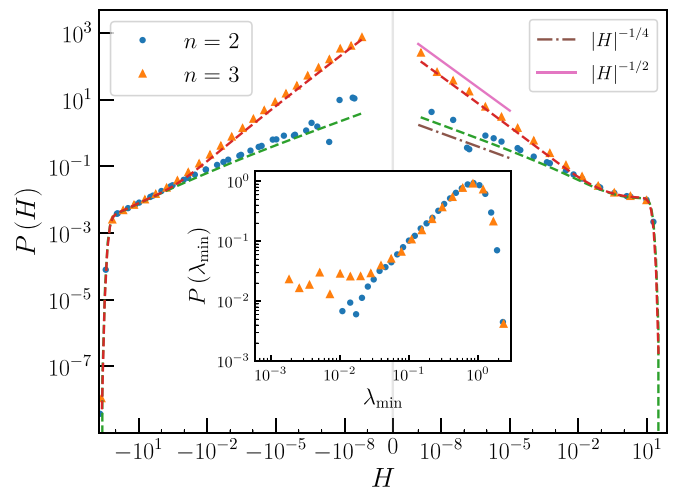


FIG. 4. Distribution of diagonal Hessian elements in the R10 system with different smoothness at cutoff $n = 2$ and 3 in two dimensions. The configurations sampled are at energy minima. The plot is in symmetric-log-log scale, showing the power-law divergence in both positive and negative H . The dashed lines represent the analytic predictions from Eq. (5), using numerically sampled radial distribution functions. Exponent of the singularity changes with the degree of smoothness n . Inset: Distribution of the minimum eigenvalue λ_{\min} of the Hessian (for system size $N = 256$), displaying significant changes with the degree of smoothness n .

For 3D systems, we choose H_{zz} and H_{xz} to represent the diagonal and off-diagonal elements, respectively. From Eq. (3) we have $H_{zz}^{3D} = -(\psi_{rr} - \frac{\psi_r}{r}) \cos^2 \phi - \frac{\psi_r}{r}$, and $H_{xz}^{3D} = -(\psi_{rr} - \frac{\psi_r}{r}) \cos \theta \sin \theta \cos \phi$. In the case of diagonal elements, it is convenient to choose $\Omega \equiv \cos \theta$, with the distribution $P_{3D}(\cos \theta) = \frac{1}{2}$ (see inset of Fig. 3). Under these conditions, the partial integrand defined in Eq. (5) is $\mathcal{P}_{zz}^{3D} = [2 \left| \frac{\partial H}{\partial \cos \theta} \right|]^{-1}$. In the case of off-diagonal elements, it is convenient to choose $\Omega \equiv \cos \phi$, and given that $P(\phi) = \frac{1}{2}$, we arrive at the exact integral form $\mathcal{P}_{xz}^{3D} = \int \pi d(\cos \theta) \left[\left| \frac{\partial H}{\partial \cos \phi} \right| \sqrt{1 - \cos^2 \phi} \right]^{-1}$. Finally, inverting the above expressions for H_{zz}^{3D} and H_{xz}^{3D} to express $\cos \theta$ and $\cos \phi$ in terms of H and r , we arrive at the simplified expressions

$$\mathcal{P}_{\alpha\beta}^{3D}(H, r) = \begin{cases} |4(H + \frac{\psi_r}{r})(\psi_{rr} - \frac{\psi_r}{r})|^{-1/2} & \alpha = \beta, \\ \frac{\kappa}{H} \int_{-1}^1 dx [x^2(1-x^2) - \kappa^2]^{-1/2} & \alpha \neq \beta \end{cases} \quad (7)$$

with $\kappa = H(\psi_{rr} - \frac{\psi_r}{r})^{-1}$. The above integral form for the off-diagonal elements has the asymptotic behavior (refer to Supplemental Material [54])

$$\mathcal{P}_{\alpha\neq\beta}^{3D}(H, r) \stackrel{\kappa \rightarrow 0}{\sim} \frac{2\kappa}{H} \log \left(\frac{4}{\kappa} \right). \quad (8)$$

The distributions of Hessian elements can now be found using these partial integrands [Eqs. (6) and (7)] in Eq. (5) along with the numerically obtained radial distribution functions, as shown in Fig. 3. We display the match between our theoretical predictions and distributions obtained from numerical simulations in Fig. 4. In the Supplemental Material [54], we additionally show a precise match between $P(H)$ obtained

analytically and numerically, for an exponentially decaying $g_2(r)$.

Asymptotic forms and singular distributions. We focus next on the behavior of $P(H)$ in the limit $H \rightarrow 0$. It is clear from the forms of the partial integrands in Eqs. (6) and (7), that they diverge as $r \rightarrow r_c$ and $H \rightarrow 0$, since $\psi_r \rightarrow 0$ and $\psi_{rr} \rightarrow 0$. Consequently, the corresponding integrals determining $P(H)$ in Eq. (5) exhibit singularities $P(H) \sim H^\gamma$ as $H \rightarrow 0$, as displayed in Figs. 1(b) and 4. We show below that the strength γ of this singularity depends on the rate of decay (i.e., smoothness n) of the interaction at cutoff.

To determine the behavior of the distribution near the singularity, we focus on the integral in Eq. (5), as we approach the cutoff $r \rightarrow r_c$. It is assumed also, that the $g_2(r)$ does not contain singularities at r_c as justified by the plot in Fig. 3. The interaction potential, smooth to n derivatives at the cutoff distance and its derivatives in the limit of $r \rightarrow r_c$, may therefore be approximated as

$$\begin{aligned} \psi(r) &= (r_c - r)^{n+1} f(r), & \psi_r/r &\approx C_1(r_c - r)^n, \\ \psi_{rr} &\approx C_2(r_c - r)^{n-1}, \end{aligned} \quad (9)$$

where $f(r)$ is a regular function, along with $C_1 = -(n+1)f(r)/r$, and $C_2 = n(n+1)f'(r)$ which vary significantly slower compared to the power-law term as $r \rightarrow r_c$. Above, in ψ_r/r , we have ignored $(r_c - r)^{n+1}f'(r)$ in comparison to $(r_c - r)^n f(r)$. Under this approximation, the singular points of $\mathcal{P}(H, r)$ in the complex- r plane are determined by the two expressions

$$(r_c - r)^n = -\frac{H}{C_1}, \quad (r_c - r)^{n-1} = -\frac{H}{C_2}. \quad (10)$$

The full structure of the poles in Eq. (10) is detailed in the Supplemental Material [54]. However, as the integral in Eq. (5) is performed over the real interval $[0, r_c]$, the new upper limit is determined by the largest positive real root of these expressions. This occurs at a value $r^* = r_c - s$, where $s \equiv s(H)$ represents the shift in the upper limit. The singular behavior in $\mathcal{P}(H, r)$ is thus determined by both the sign of H , and the signs of the first two derivatives of the potential (C_1 and C_2), as the cut-off distance $r \rightarrow r_c$ is approached.

In order to analyze the asymptotic forms of $P(H)$ in Eq. (5) as $H \rightarrow 0$, we define a small variable ϵ as a distance to r^* at a given value of H , $\epsilon = (r_c - s) - r$. The derivatives of the potential described in Eq. (9) can then be written as

$$\psi_r/r \approx C_1(\epsilon + s)^n, \quad \psi_{rr} \approx C_2(\epsilon + s)^{n-1}. \quad (11)$$

We can now extract the asymptotic behavior of $P(H)$ using this approximation in the partial integrands in Eqs. (6) and (7). The behavior of these integrands depends on the relative signs of H and the interaction potential near cutoff $\psi_\delta \equiv \psi(r_c - \delta)$ with $\delta/r_c \ll 1$. Below, we present the analysis for the diagonal elements in 2D, with the details of all cases presented in the Supplemental Material [54]. Using Eq. (11) in Eq. (6), for $H \rightarrow 0$, $\epsilon \rightarrow 0$, we have

$$\mathcal{P}_{\alpha\alpha}^{2D}(H, \epsilon) \sim \{[H + C_1(\epsilon + s)^n][H + C_2(\epsilon + s)^{n-1}]\}^{-1/2}. \quad (12)$$

We can extract the limiting behavior of $P(H)$ by identifying the dominant contribution from the above expression to the

integral in Eq. (5). There exist up to three regimes of ϵ in terms of the behavior of the partial integrand in Eq. (12): (i) $[0, H^{1/n-1})$, (ii) $[H^{1/n-1}, H^{1/n})$, and (iii) $[H^{1/n}, \infty)$, depending on the shift $s(H)$ (refer to Supplemental Material [54]). For the case $H \times \psi_\delta > 0$, contribution of the integral over the last interval dominates, with $P(H) \sim \int_{H^{1/n}}^{\infty} \epsilon^{-n+1/2} = \epsilon^{-n+3/2} \Big|_{H^{1/n}}^{\infty}$. Therefore, we arrive at the asymptotic form $\mathcal{P}_{\alpha\alpha}^{2D}(H) \sim H^{-1+(3/2n)}$. Our results for all cases are summarized in Table I. Remarkably, although the expressions in Eqs. (6) and (7) have very different forms, they yield exactly the same results for the singularities in both 2D and 3D.

Numerical simulations. In order to verify our predictions, we have performed extensive numerical simulations of structural glass formers, in 2D as well as 3D. We simulate a binary mixture of purely repulsive particles of type A and B (refer to Supplemental Material [54]). The A-B interactions are illustrated in Fig. 2. High-temperature molecular dynamics simulations were utilized to generate independent, uncorrelated configurations of particles, and sample their inherent structures by locating the nearest local minimum via the conjugate-gradient minimization. We then evaluate the Hessian elements between particles within interacting range of each other. In Fig. 4 we plot the numerically sampled distributions of the diagonal Hessian elements for A-B interactions in 2D systems for $n = 2$ and $n = 3$, along with our theoretical predictions (dashed lines) using Eq. (5) in Eq. (6), displaying near-perfect agreement. These distributions diverge as $H \rightarrow 0^+$ with the exponents $-\frac{1}{4}$ for $n = 2$ and $-\frac{1}{2}$ for $n = 3$, as predicted in Table I.

Finally, we turn our attention to the vibrational properties of the system, that are probed through the eigenvalue spectrum of the Hessian matrix. We test the sensitivity of low-lying eigenvalues to the smoothness of the potential, and consequently, the power of the singularity in $P(H)$, by analyzing the distribution of the minimum eigenvalue, λ_{\min} . Our results for the short-ranged R10 glass model, displayed in the inset of Fig. 4, show a significant divergence at low values, between distributions for two values of smoothness.

Discussion. We have presented analytic results for the distribution of Hessian elements in disordered amorphous media in 2D and 3D, and verified them with extensive numerical simulations. Our treatment is quite general, relying only on the isotropy of the underlying amorphous medium, and can be extended to other systems displaying such disorder. Additionally, we have shown that the Hessian matrices of amorphous materials display a preponderance of small elements, characterized by a singularity whose strength depends on the smoothness of the interaction potential at the cut-off distance. Remarkably, the results for the singularities are exactly the same in both 2D and 3D, a fact that warrants deeper investigation. We have also shown numerically that such singularities have crucial implications for the low-lying eigenvalues of the Hessian matrix that govern the stability or fragility of amorphous solids, highlighting their sensitivity to the small, nonzero elements in the Hessian matrix. Our results are particularly relevant for numerical studies of glasses, where the degree of smoothness in interaction potentials have been shown to affect vibrational properties [55]. The limit

where such interaction potentials display sharp cutoffs are typically used in the study of jamming transitions [56–59], and it would be interesting to study the effect of smoothness in the potential on the properties of such systems. Finally, it would also be interesting to extend our analytic results to construct bounds on the vibrational density of states of amorphous systems [60].

Acknowledgments. We thank Edan Lerner, Prathyush Manchala, Mustansir Barma, Daan Frenkel, Srikanth Sastry,

Chandan Dasgupta, Satya Majumdar, Kedar Damle, and Deepak Dhar for useful discussions. V.V.K. thanks Council of Scientific and Industrial Research, India for support from the Shyama Prasad Mukherjee Fellowship (SPM-07/1142(0228)/2015-EMR-1). S.K. would like to acknowledge the support from Swarna Jayanti Fellowship Grants No. DST/SJF/PSA-01/2018-19 and No. SB/SFJ/2019-20/05. This project was funded by intramural funds at TIFR Hyderabad from the Department of Atomic Energy (DAE).

-
- [1] C. A. Angell, *J. Phys. Chem. Solids* **49**, 863 (1988).
 [2] T. R. Kirkpatrick and D. Thirumalai, *Phys. Rev. B* **36**, 5388 (1987); *Phys. Rev. A* **37**, 4439 (1988); *Phys. Rev. B* **37**, 5342 (1988); *J. Phys. A: Math. Gen.* **22**, L149 (1989).
 [3] P. G. Debenedetti, *Metastable Liquids: Concepts and Principles* (Princeton University Press, Princeton, NJ, 1996).
 [4] S. P. Das, *Rev. Mod. Phys.* **76**, 785 (2004).
 [5] W. Götze, in *International Series of Monographs on Physics* (Oxford University Press, Oxford, 2008), Vol. 143.
 [6] H. Shintani and H. Tanaka, *Nat. Mater.* **7**, 870 (2008).
 [7] L. Berthier and G. Biroli, *Rev. Mod. Phys.* **83**, 587 (2011).
 [8] P. G. Wolynes and V. Lubchenko, *Structural Glasses and Supercooled Liquids: Theory, Experiment, and Applications* (Wiley, New York, 2012).
 [9] S. Karmakar, C. Dasgupta, and S. Sastry, *Annu. Rev. Condens. Matter Phys.* **5**, 255 (2014).
 [10] S. Karmakar, C. Dasgupta, and S. Sastry, *Rep. Prog. Phys.* **79**, 016601 (2015).
 [11] S. Sastry, P. G. Debenedetti, and F. H. Stillinger, *Phys. Rev. E* **56**, 5533 (1997).
 [12] C. A. Angell, Y. Yue, L.-M. Wang, J. R. D. Copley, S. Borick, and S. Mossa, *J. Phys.: Condens. Matter* **15**, S1051 (2003).
 [13] A. Zaccone, *J. Phys.: Condens. Matter* **32**, 203001 (2020).
 [14] C. A. Angell and K. J. Rao, *J. Chem. Phys.* **57**, 470 (1972).
 [15] M. Goldstein, *J. Chem. Phys.* **64**, 4767 (1976).
 [16] U. Buchenau, N. Nücker, and A. J. Dianoux, *Phys. Rev. Lett.* **53**, 2316 (1984).
 [17] B. Rufflé, M. Foret, E. Courtens, R. Vacher, and G. Monaco, *Phys. Rev. Lett.* **90**, 095502 (2003).
 [18] V. L. Gurevich, D. A. Parshin, and H. R. Schober, *Phys. Rev. B* **67**, 094203 (2003).
 [19] B. Rufflé, G. Guimbretière, E. Courtens, R. Vacher, and G. Monaco, *Phys. Rev. Lett.* **96**, 045502 (2006).
 [20] A. Moriel, G. Kapteijns, C. Rainone, J. Zylberg, E. Lerner, and E. Bouchbinder, *J. Chem. Phys.* **151**, 104503 (2019).
 [21] G. Monaco and S. Mossa, *Proc. Natl. Acad. Sci. U.S.A.* **106**, 16907 (2009).
 [22] G. Monaco and V. M. Giordano, *Proc. Natl. Acad. Sci. U.S.A.* **106**, 3659 (2009).
 [23] E. DeGiuli, A. Laversanne-Finot, G. Düring, E. Lerner, and M. Wyart, *Soft Matter* **10**, 5628 (2014).
 [24] P. Charbonneau, E. I. Corwin, G. Parisi, A. Poncet, and F. Zamponi, *Phys. Rev. Lett.* **117**, 045503 (2016).
 [25] E. Lerner, G. Düring, and E. Bouchbinder, *Phys. Rev. Lett.* **117**, 035501 (2016).
 [26] G. Kapteijns, E. Bouchbinder, and E. Lerner, *Phys. Rev. Lett.* **121**, 055501 (2018).
 [27] L. Wang, A. Ninarello, P. Guan, L. Berthier, G. Szamel, and E. Flenner, *Nat. Commun.* **10**, 26 (2019).
 [28] M. Shimada, H. Mizuno, L. Berthier, and A. Ikeda, *Phys. Rev. E* **101**, 052906 (2020).
 [29] E. Stanifer, P. K. Morse, A. A. Middleton, and M. L. Manning, *Phys. Rev. E* **98**, 042908 (2018).
 [30] Y. M. Beltukov and D. A. Parshin, *Phys. Solid State* **53**, 151 (2011).
 [31] M. L. Manning and A. J. Liu, *Europhys. Lett.* **109**, 36002 (2015).
 [32] Y. M. Beltukov, V. I. Kozub, and D. A. Parshin, *Phys. Rev. B* **87**, 134203 (2013).
 [33] M. Baggioli, R. Milkus, and A. Zaccone, *Phys. Rev. E* **100**, 062131 (2019).
 [34] D. A. Conyuh, Y. M. Beltukov, and D. A. Parshin, *J. Phys.: Conf. Ser.* **929**, 012031 (2017).
 [35] C. Brito, O. Dauchot, G. Biroli, and J.-P. Bouchaud, *Soft Matter* **6**, 3013 (2010).
 [36] A. Altieri, An exactly solvable model: The perceptron, *Jamming and Glass Transitions: In Mean-Field Theories and Beyond* (Springer, New York, 2019), pp. 65–113.
 [37] A. Maradudin and G. H. Weiss, *J. Soc. Indust. Appl. Math.* **6**, 302 (1958).
 [38] V. Gurarie and J. T. Chalker, *Phys. Rev. B* **68**, 134207 (2003).
 [39] F. P. C. Benetti, G. Parisi, F. Pietracaprina, and G. Sicuro, *Phys. Rev. E* **97**, 062157 (2018).
 [40] A. Cavagna, I. Giardina, and G. Parisi, *Phys. Rev. Lett.* **83**, 108 (1999).
 [41] B. J. Huang and T.-M. Wu, *Phys. Rev. E* **79**, 041105 (2009).
 [42] C. Kittel, *Introduction to Solid State Physics*, 8th ed. (Wiley New York, 2004).
 [43] N. W. Ashcroft and N. D. Mermin, *Solid State Physics* (Cengage Learning, Boston, 1976).
 [44] A. Ghosh, V. K. Chikkadi, P. Schall, J. Kurchan, and D. Bonn, *Phys. Rev. Lett.* **104**, 248305 (2010).
 [45] X. Wang, S. Ramírez-Hinestrosa, J. Dobnikar, and D. Frenkel, *Phys. Chem. Chem. Phys.* **22**, 10624 (2020).
 [46] O. Dauchot, S. Karmakar, I. Procaccia, and J. Zylberg, *Phys. Rev. E* **84**, 046105 (2011).
 [47] S. Karmakar, E. Lerner, and I. Procaccia, *Physica A* **391**, 1001 (2012).
 [48] C. Rainone, E. Bouchbinder, and E. Lerner, *Proc. Natl. Acad. Sci. U.S.A.* **117**, 5228 (2020).
 [49] C. Maloney and A. Lemaître, *Phys. Rev. Lett.* **93**, 195501 (2004).

- [50] C. E. Maloney and A. Lemaître, *Phys. Rev. E* **74**, 016118 (2006).
- [51] R. Dasgupta, S. Karmakar, and I. Procaccia, *Phys. Rev. Lett.* **108**, 075701 (2012).
- [52] D. Frenkel and B. Smit, *Understanding Molecular Simulation: From Algorithms to Applications*, 2nd ed. (Elsevier, New York, 2002).
- [53] S. Karmakar, E. Lerner, and I. Procaccia, *Phys. Rev. E* **82**, 026105 (2010), Appendix C.
- [54] See Supplemental Material at <http://link.aps.org/supplemental/10.1103/PhysRevResearch.2.042025> for details, which includes Refs. [61–68].
- [55] M. Shimada, H. Mizuno, and A. Ikeda, *Phys. Rev. E* **97**, 022609 (2018).
- [56] C. S. O’Hern, L. E. Silbert, A. J. Liu, and S. R. Nagel, *Phys. Rev. E* **68**, 011306 (2003).
- [57] L. E. Silbert, A. J. Liu, and S. R. Nagel, *Phys. Rev. E* **73**, 041304 (2006).
- [58] K. Ramola and B. Chakraborty, *J. Stat. Mech.* (2016) 114002.
- [59] K. Ramola and B. Chakraborty, *Phys. Rev. Lett.* **118**, 138001 (2017).
- [60] R. A. Horn and C. R. Johnson, *Matrix Analysis* (Cambridge University Press, Cambridge, UK, 2012), Chap. 6.
- [61] S. Plimpton, *J. Comput. Phys.* **117**, 1 (1995).
- [62] Large-scale Atomic/Molecular Massively Parallel Simulator, Sandia National Laboratories (2003), Versions: 12Dec2018, 5Jun2019, <https://lammmps.sandia.gov>.
- [63] E. Anderson, Z. Bai, C. Bischof, S. Blackford, J. Demmel, J. Dongarra, J. Du Croz, A. Greenbaum, S. Hammarling, A. McKenney, and D. Sorensen, *LAPACK Users’ Guide*, 3rd ed. (Society for Industrial and Applied Mathematics, Philadelphia, PA, 1999).
- [64] Intel, Math Kernel Library, 2019.
- [65] Wolfram Research, Inc., Mathematica, version: 12.0, 2019.
- [66] SciPy, version: 1.3.0: Open source scientific tools for Python (2001), <https://www.scipy.org/>.
- [67] J. D. Hunter, *Comput. Sci. Eng.* **9**, 90 (2007).
- [68] Matplotlib, version: 3.1.2 (2019), [10.5281/zenodo.3563226](https://doi.org/10.5281/zenodo.3563226).